Results in Chemistry 23 (2026) 103144

Contents lists available at ScienceDirect

Results in Chemistry

journal homepage: www.sciencedirect.com/journal/results-in-chemistry

The photoluminescence degradation of InP/ZnSe$_x$S$_{1-x}$/ZnS quantum dot films

Min Fu [a], Alex Walton [b], Liam Dwyer [c], Xinhui Lan [a], Stephen D. Evans [a], Kevin Critchley [a,*]

[a] School of Physics and Astronomy, University of Leeds, Leeds LS2 9JT, United Kingdom
[b] Department of Chemistry and Photon Science Institute, The University of Manchester, Oxford Road, Manchester M13 9PL, UK
[c] Department of Materials and Henry Royce Institute, The University of Manchester, Oxford Road, Manchester M13 9PL, UK

ARTICLE INFO

Keywords:
Air stability
Photoluminescence degradation
Indium phosphide
Quantum dot films
Encapsulation

ABSTRACT

InP/ZnSe$_x$S$_{1-x}$/ZnS quantum dots (QDs) are promising candidates for next-generation electroluminescent devices. However, their photoluminescence (PL) irreversibly quenches over time under ambient conditions, limiting open-air manufacturing techniques such as inkjet printing. While most degradation studies have focused on QD dispersions rather than the QD films, critical for colour conversion, electroluminescent, and sensor devices, remain less understood. In this work, we investigated the PL quenching of InP/ZnSe$_x$S$_{1-x}$/ZnS QD films by varying the film thickness, humidity level, and temperature. We find that higher relative humidity slows PL quenching, likely due to photoinduced fluorescence enhancement. Increasing QD film thickness from 19 nm to 100 nm extended the PL degradation half-life ($\tau_{1/2}$) by 5.6 times. Heating above 100 °C, under vacuum (0.1 mbar), accelerates degradation due to stripping of ligands and trap state formation from strain and atomic mobility. In-situ near-ambient X-ray photoelectron spectroscopy reveals oxidation products such as In_2O_3, $InPO_x$, ZnO, SeO_2, and SO_x^-. Applying a 47-nm-thick polymethyl methacrylate barrier increases $\tau_{1/2}$ by 12-fold, significantly enhancing air stability. These findings provide insights into degradation mechanisms and strategies for improving the durability of QD films in practical applications.

1. Introduction

Quantum dots (QDs) are emerging as key materials in advanced optoelectronic devices, for example, photodetectors [1], solar cells [2], and QD-based light-emitting diodes (QLEDs) [3]. Among them, InP QDs are an alternative to Cd-based QDs, with high photoluminescence (PL) quantum yield (PLQY), narrow emission linewidth, and reduced toxicity [4,5]. However, QDs are susceptible to degradation due to diverse molecular interactions with oxygen and water under light. Exposure to oxygen and moisture, especially under illumination, can lead to physical and/or chemical adsorption on the QD surface, triggering photoactivation [6], photooxidation [7], and photocorrosion [8]. These processes degrade optical performance by introducing trap states and non-radiative recombination pathways. In particular, In and P are easily oxidized to form In_2O_3 and $InPO_x$, which degrade the QD PL properties quickly under ambient atmosphere, significantly diminishing PL efficiency under ambient conditions [9,10].

While the degradation of CdSe QDs that combines oxygen, water vapor, and illumination has been extensively studied [11,12], the effects of oxygen and/or moisture on the PL quenching and chemical state changes in InP QD films, particularly without UV illumination, remain poorly understood. Recent work by Baek et al. investigated structural defect formation, such as ZnO, in InP/ZnSe/ZnS QD dispersion during UV-facilitated oxidation using high-resolution transmission electron microscopy (TEM) [13]. Furthermore, InP-based QLEDs assembled by open-air manufacturing technology (e.g., inkjet printing) exhibit inferior electrical performance than those fabricated in the ambient atmosphere [3]. A deeper understanding of degradation processes in InP QD films is therefore essential to address these performance limitations and enable scalable, ambient-condition fabrication.

The large lattice strain between InP and ZnS (7.6%) causes anomalous interfacial reconstruction and surface defects, limiting its ability to passivate trap states at the interface between the core and the shell [14]. Introducing an alloyed ZnSe$_x$S$_{1-x}$ middle shell can further reduce the misfit strain to below 3.4% and promote the PLQY to beyond 90% [15,16]. Despite these improvements, the PL of core-shell InP/ZnSe$_x$S$_{1-x}$/ZnS QDs can still be quenched in ambient conditions, with the shell passivation only delaying this process [17]. Apart from ZnS shell

* Corresponding author.
E-mail address: k.critchley@leeds.ac.uk (K. Critchley).

https://doi.org/10.1016/j.rechem.2026.103144
Received 6 January 2026; Accepted 16 February 2026
Available online 19 February 2026

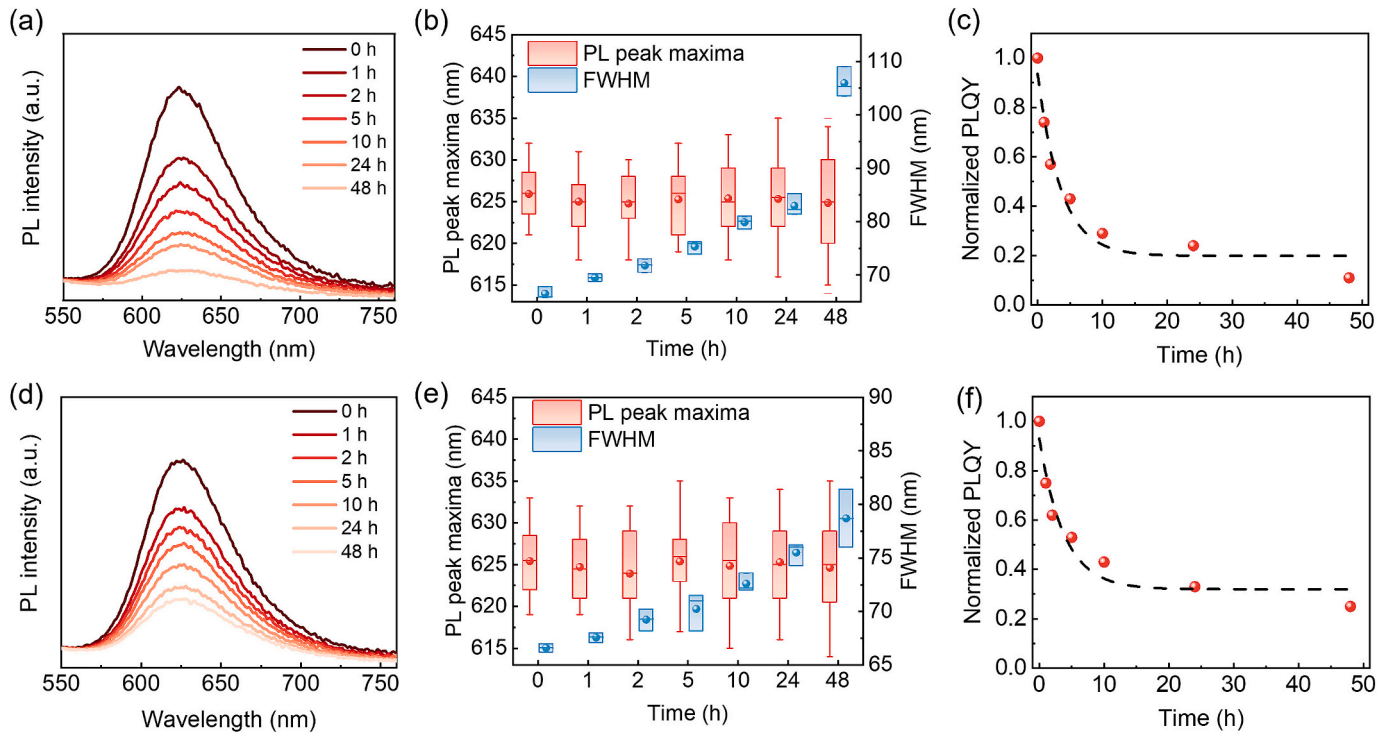

Fig. 1. The evolution of PL emission spectra, corresponding PL peak maxima and FWHM, and normalized PLQY of 19-nm-thick QD films under different RH over time at 22 °C. RH of (a–c) 35% and (d–f) 55%. The black dashed lines in (c) and (f) are fitting curves of the exponential degradation function.

Table 1
The degradation half-life of QD films under different experimental conditions.

	RH (%)	Temperature (°C)	t_{QD} (nm)	L (nm)	$\tau_{1/2}$ (h)	I_∞
Ambient atmosphere	55	22	101 ± 4	N.A.	17.2	0.4
	55	22	48 ± 2	N.A.	5.9	0.2
	55	22	19 ± 1	N.A.	2.6	0.3
	55	22	19 ± 1	47 ± 6	33.5	0.2
	55	22	19 ± 1	20 ± 1	15.0	0.2
	35	22	19 ± 1	N.A.	2.5	0.2
Vacuum (0.1 mbar)	6	22	19 ± 1	N.A.	N.A.	N. A.
	6	50	19 ± 1	N.A.	2.7	0.5
	6	100	19 ± 1	N.A.	2.2	0.4

coating, researchers have proposed other strategies to mitigate QD film degradation, such as ligand engineering [18] and surface encapsulation [19]. Encapsulating the QD layer with a thin polymer layer can improve air/thermal stability by isolating QDs from the environment [20,21]. For example, polymethylmethacrylate (PMMA) is an excellent organic optical material, offering minimal chromatic dispersion, good environmental inertness, and high transparency across the visible spectrum [22]. Dai et al. spin-coated a thin PMMA layer between the QD layer and electron transport layer to balance the charge injection in QLEDs, thus dramatically boosting the external quantum efficiency to 20.5% [23]. Additionally, QD-PMMA nanocomposites have been used in active planar waveguides [24] and the alleviation of the coffee ring effect in inkjet printing of QLEDs [25].

In this study, the degradation of InP/ $ZnSe_xS_{1-x}$/ZnS QD films by oxygen, water, and heat was characterized using fluorescence spectroscopy and in-situ near-ambient X-ray photoelectron spectroscopy (NAP-XPS). We studied the PL quenching of InP/$ZnSe_xS_{1-x}$/ZnS QD films in the dark over time by tuning the film thickness (19 nm, 48 nm, and 100 nm), relative humidity (RH: 6%, 35%, and 55%), and temperature (22 °C, 50 °C, and 100 °C). Chemical variations were detected by NAP-XPS under oxygen or/and moisture exposure at room temperature (RT) and 100 °C. To improve the air stability of QD films, a thin encapsulation layer of spin-coated PMMA, with thicknesses of 20 nm and 47 nm, was employed to protect QD films from oxygen and moisture.

2. Experimental

2.1. Materials

Indium chloride ($InCl_3$, 99.99%), magnesium chloride hexahydrate ($MgCl_2{\cdot}6H_2O$), magnesium nitrate hexahydrate ($Mg(NO_3)_2{\cdot}6H_2O$), and zinc chloride ($ZnCl_2$, 98 + %) were purchased from Thermo Fisher Scientific. Selenium powder (Se, 99.9%) was purchased from Alfa Aesar. Isopropyl alcohol (IPA), acetone, and oleic acid (OA, 97%) were purchased from VWR Chemicals. Zinc stearate ($Zn(St)_2$), squalane (SQL), zinc acetate ($Zn(acet)_2$), trioctylphosphine (TOP, >97%), octanethiol (OT, >98.5%), oleylamine (OAm, 70%), tris-(dimethylamino)phosphine ($(DMA)_3P$, 97%), sulfur powder (S, 99.98%), hexane, and octane were purchased from Sigma-Aldrich. PMMA (M_w = 100 k) was purchased from Polysciences.

2.2. Synthesis of multi-shelled red InP/$ZnSe_xS_{1-x}$/ZnS QDs

0.45 mmol $InCl_3$ and 2.2 mmol $ZnCl_2$ were dissolved in 6 mL OAm and degassed at 120 °C for 1 h. 0.35 mL $(DMA)_3P$ was then quickly injected into the solution at 180 °C under an N_2 atmosphere and reacted for 10 min to form the InP core. Next, 1.0 mL Se-TOP solution (0.12 mol/L), 4.0 mL $Zn(St)_2$-SQL solution (4.74 mol/L), the mixture of 0.5 mL Se-TOP (0.12 mol/L) and 1.0 mL S-TOP solution (2.0 mol/L), 4.0 mL $Zn(St)_2$-SQL solution, the mixture of 0.17 mL Se-TOP (0.12 mol/L) and 2.0 mL S-TOP solution (2.0 mol/L), were injected into the core solution in turn and reacted at 200 °C, 220 °C, 240 °C, 260 °C, and 280 °C, respectively, for 30 min. 4.0 mL $Zn(St)_2$-SQL solution was injected and reacted at 300 °C for 1 h. Subsequently, 5.0 mL OT was injected and reacted at 190 °C for 60 min. 3.0 mL $Zn(acet)_2$-OA solution (1.0 mol/L) was then injected into the flask at 190 °C for 2 h and cooled to RT after the reaction. The as-synthesized InP/$ZnSe_xS_{1-x}$/ZnS QD dispersion was

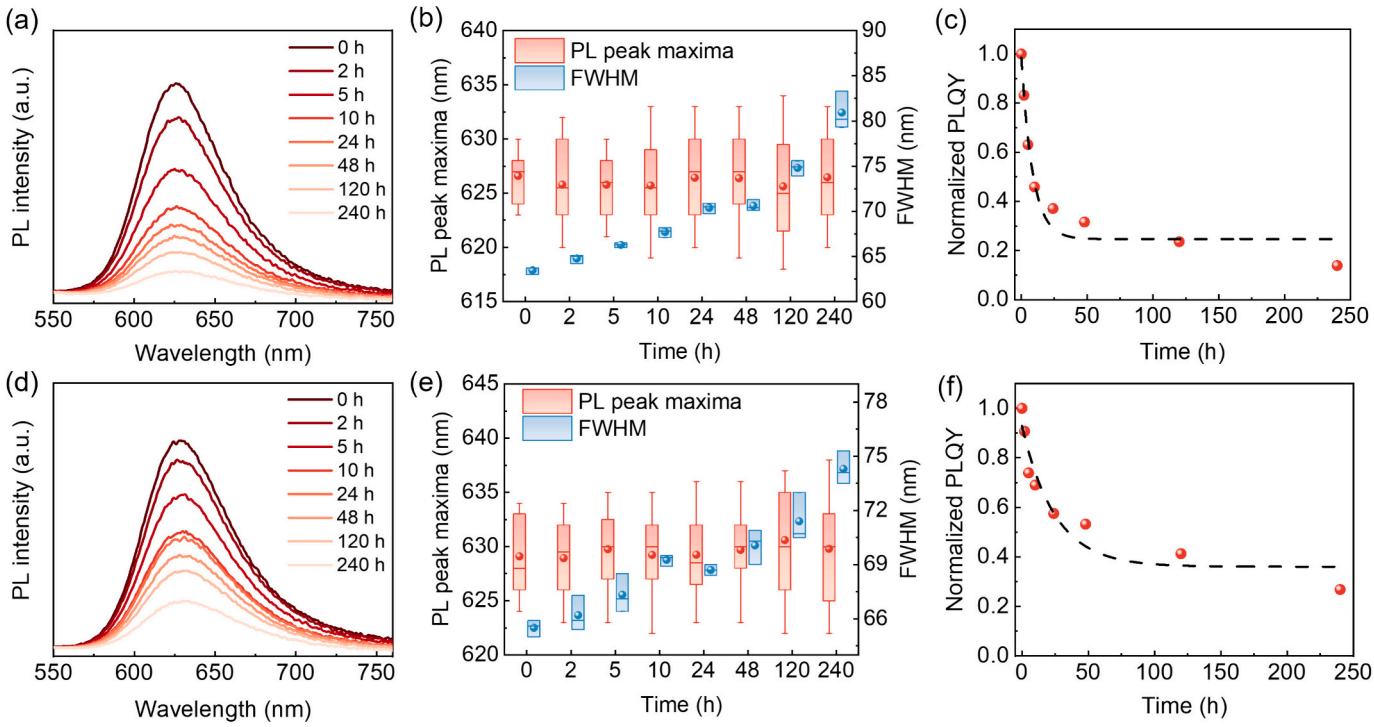

Fig. 2. The evolution of PL emission spectra, corresponding PL peak maxima and FWHM, and normalized PLQY of QD films with different thicknesses under the RH of 55% over time at 22 °C. t_{QD} of (a–c) 48 nm and (d–f) 101 nm. The black dashed lines in (c) and (f) are fitting curves of the exponential degradation function.

diluted by hexane and centrifuged at 15,000 RCF for 10 min under an ambient atmosphere. IPA with three times the volume of hexane was then added to the supernatant, and the pellets were collected after centrifugation at 15,000 RCF for 10 min. The cleaning steps were repeated at least three times, and the purified QDs were dispersed in octane.

2.3. Spin coating of QD films and PMMA films with various thicknesses

The stock QD dispersion was diluted to 15, 30, and 60 mg/mL by octane and then spin-coated with different spin speeds for 50 s on silicon wafers. PMMA was dissolved in acetone with concentrations of 0.05, 0.5, and 2 mg/mL and spin-coated with various spin speeds for 40 s on silicon wafers. The thicknesses of QD films and PMMA films (L) spin-coated by different spin speeds were summarized in Table S1 and Table S4, respectively. For PMMA-encapsulated QD films, the PMMA solution with concentrations of 0.05 and 0.5 mg/mL was spin-coated at 4000 RPM on the 19-nm-thick QD films in the glove box, respectively.

2.4. Characterization

The steady-state fluorescence and PLQY of QD films were measured using a fluorimeter with an integrated sphere (FLS980, Edinburgh Instrument), and the excitation wavelength set to 400 nm. The time-resolved PL measurements were performed using the FLS980 spectrometer equipped with a pulsed diode laser source (EPL-470) and detected using time-correlated single-photon counting (TCSPC). The time-resolved PL data were fitted by a biexponential function. The absorbance was measured by a UV–Vis spectrometer (Cary5000 UV–Vis, Agilent) from 350 to 700 nm. Before NAP-XPS measurements, 19-nm-thick QD films were spin-coated in the glove box and then transferred to the NAP-XPS in an inert atmosphere to ensure in-situ experiments started from $t = 0$. The NAP-XPS was performed in a SPECS NAP-XPS system consisting of a UHV ($\sim 5 \times 10^{-10}$ mbar) analysis chamber, NAP cell, and e-beam heating capability. At the start and end of experiments, monochromated Al Kα X-rays (14.5 kV, 120 W) were focused to a spot of 1 mm in diameter in the UHV chamber. NAP-XPS experiments were performed by placing QD films inside a NAP cell with a 300-μm aperture, which allowed pressures within the cell to reach 3 mbar of oxygen, 3 mbar of moisture (RH: ~10%), or 6 mbar of both oxygen and moisture (3 mbar of each). Scanning was focused to a 0.3 mm spot (14.5 kV, 25 W) and performed cyclically to allow the identification of any changes in the QD films at RT and 100 °C, respectively, for about 8 h. XPS data were analyzed using the CasaXPS software, and the binding energy scale was calibrated from hydrocarbon ligands using the C-C/C-H peak at 284.8 eV. All photoelectron binding energies are quoted to a precision of ±0.05 eV. Regions and components were fitted to each peak with the appropriate relative sensitivity factors taken from the Scofield library file within CasaXPS. Baseline fitting of photoelectron peaks was performed using a Shirley-type baseline. The peak positions and areas were optimized by a weighted least-squares fitting method using 70% Gaussian and 30% Lorentzian line shapes. The thicknesses of spin-coated QD films and PMMA films on the silicon wafer were characterized by the ellipsometer (M-2000, J A Woollam) using a wavelength range of 250 to 1000 nm. The angles of light incidence were operated between 50° and 75° relative to the surface normal in steps of 5°. Ellipsometric data were analyzed on the CompleteEase software and fitted by the Cauchy model initially in the transparent region (>600 nm) with acceptable mean square error (MSE <10). Then converted to the B-spline model to expand the fitting range down to 250 nm. Finally, the model was converted to the Gen-Osc model and fitted by Tauc-Lorentz oscillators. The relative humidity of 35% and 55% was controlled by saturated salt solutions of $MgCl_2{\cdot}6H_2O$ and $Mg(NO_3)_2{\cdot}6H_2O$, respectively, with a weight ratio of 80% [26]. The morphology of QD and PMMA films with different thicknesses was characterized using tapping mode atomic force microscope (Fastscan, Bruker). The RH and temperature were monitored using a digital temperature humidity meter with ±5% accuracy of RH and ± 1 °C accuracy of temperature.

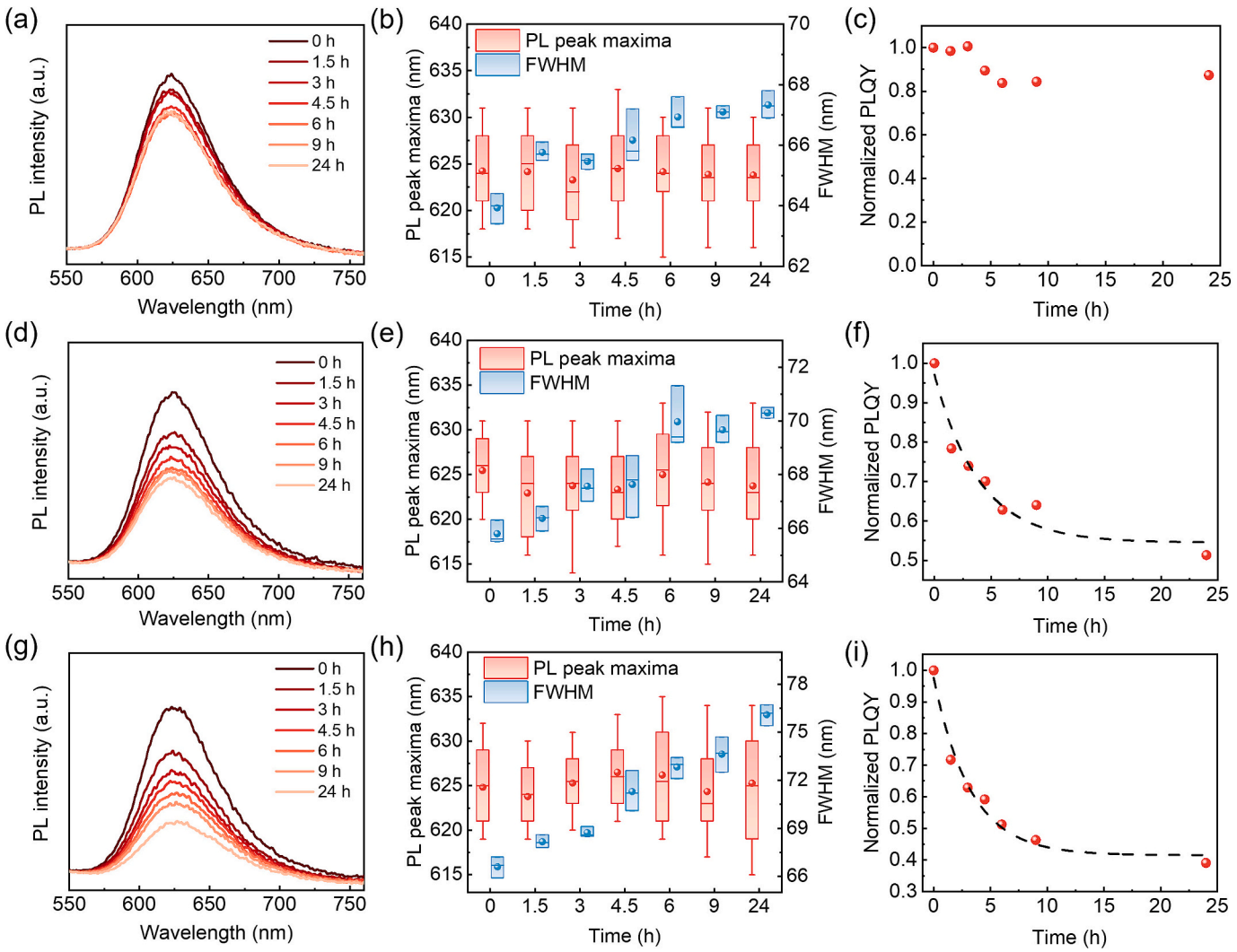

Fig. 3. The evolution of PL emission spectra, corresponding PL peak maxima and FWHM, and normalized PLQY of 19-nm-thick QD films under vacuum (0.1 mbar) over time at different temperatures. (a–c) 22 °C, (d–f) 50 °C, and (g–i) 100 °C. The black dashed lines in (c), (f), and (i) are fitting curves of the exponential degradation function.

3. Results and discussion

3.1. The effect of relative humidity on the PL quenching

The synthesis protocol for the QDs is detailed in the Methods. The synthesized InP/$ZnSe_xS_{1-x}$/ZnS QD dispersion showed a PL peak maxima at 615 nm, with a full width at half-maximum (FWHM) of 58 nm (Fig. S1). The measured PLQY of 81% ± 2% indicated that the passivation of the core with the shell was successful and resulted in high-quality QDs of similar quality to other reports [10,27]. The QD films were smooth after spin coating on the glass coverslip, without pinholes (Fig. S2 and Table S1). The emission spectra of QD films red-shifted by 10 nm to approximately 625 nm compared to the dispersion, as shown in Fig. 1(a). This red-shifting is commonly observed in close-packed QD films and is often attributed to inter-QD energy transfer processes, including Förster resonance energy transfer (FRET) [28,29]. In close-packed QD solids exciton migration from smaller to larger QDs has been widely discussed as a possible consequence of inter-QD coupling. The emission peak shift is accompanied by a significant reduction in the absolute PLQY of 19-nm-thick QD films to 18 ± 2% under 35% RH (Fig. S1b), indicating the introduction of non-radiative decay pathways in the film. Consistent with this, the average lifetime of 19-nm-thick QD film (50.9 ns) is significantly shorter than that of QD dispersion (72.0 ns), as shown in Fig. S1c. Rate analysis reveals a strong increase in the non-radiative decay rate together with a reduction in the radiative rate in the film, suggesting that exciton migration and/or trap-assisted quenching dominate exciton relaxation in the close-packed films. The PLQY of the QD film is comparable to the reported values in the literature [30,31], but is inferior to that of state-of-the-art InP QD films (58%) [32]. After 48 h of storage in the dark, the QD films became almost non-emissive. The PL peak maxima position remained nearly unchanged, but the FWHM greatly increased by 39 nm (Fig. 1(b)). Reduced emission and broader emission peaks are consistent with the formation of shallow hole traps which are attributed to incomplete surface passivation and structural disorder induced by lattice defects [33]. Triplet oxygen can directly chemisorb onto under-coordinated In or P sites, leading to the formation of interfacial oxides and ligand desorption or oxidation [10]. The oxidized regions introduce structural defects within the QD lattice or at the core/shell interface, excitons (electron-hole pairs) generated in the QD can become trapped in these newly formed surface defects instead of recombining radiatively, thus reducing the PL intensity. The PL degradation half-life ($\tau_{1/2} = k \ln 2$, Fig. 1(c) and Table 1) was calculated to be 2.5 h and was fitted by an exponential degradation function,

$$I(t) = I_0 e^{-\frac{t}{k}} + I_\infty \quad (1)$$

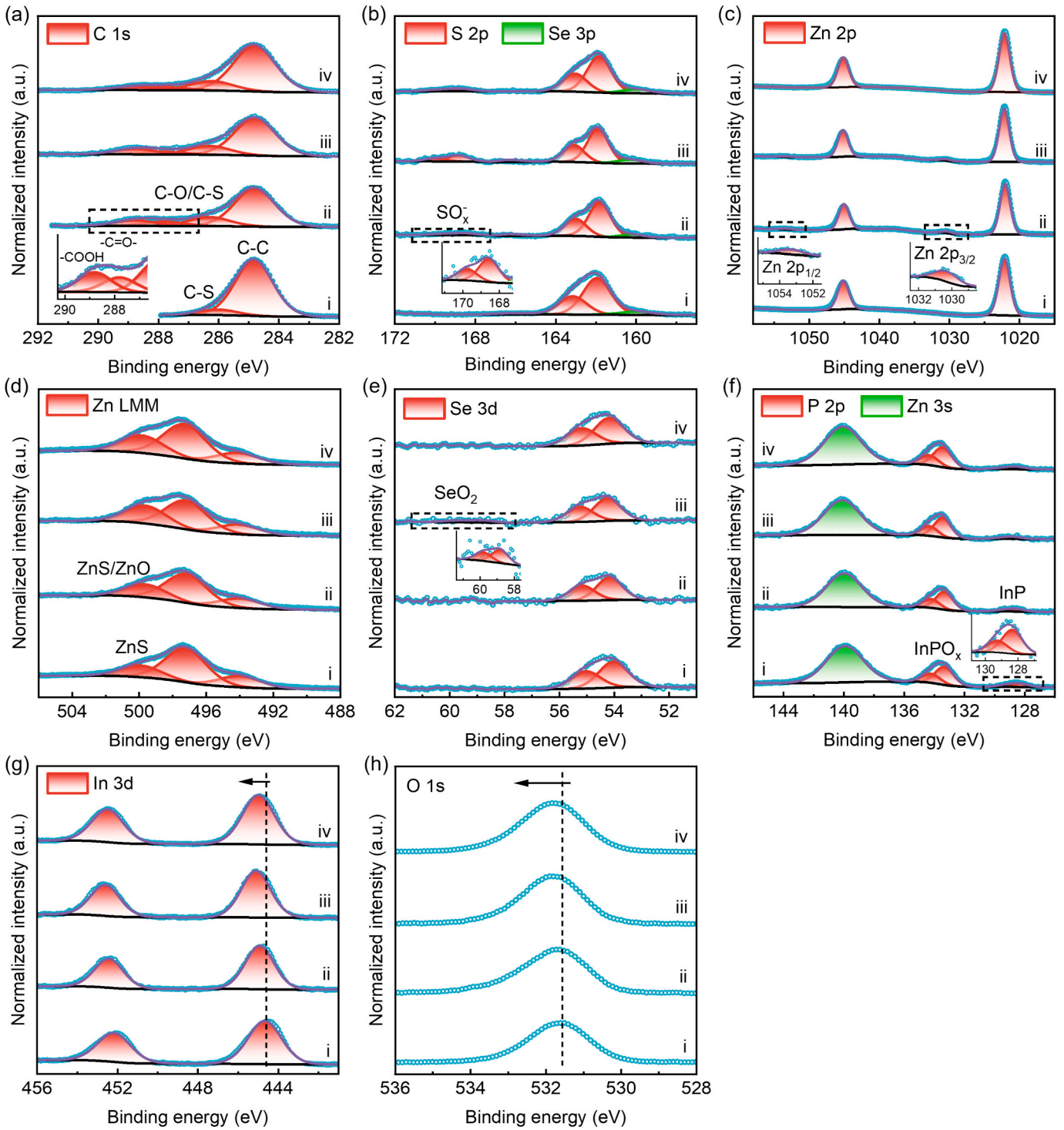

Fig. 4. NAP-XPS spectra of (a) C 1 s, (b) S 2p & Se 3p, (c) Zn 2p, (d) Zn LMM, (e) Se 3d, (f) P 2p & Zn 3 s, (g) In 3d, and (h) O 1 s of 19-nm-thick QD films under different oxygen exposure conditions. i – UHV before oxygen exposure, ii – 3 mbar oxygen exposure at RT, iii – 3 mbar oxygen exposure at 100 °C, iv – UHV after oxygen exposure. The black, purple, and cyan dotted lines represent the background, envelop, and raw data, respectively. (For interpretation of the references to colour in this figure legend, the reader is referred to the web version of this article.)

where I_0, t, k, and I_∞ are the initial PLQY, time, degradation rate, and a constant, respectively.

Under a higher RH of 55%, QD films exhibited a slower degradation rate and smaller change of FWHM (Fig. 1(d)–1(f)). The initial absolute PLQY increased by about 4%, and $\tau_{1/2}$ was slightly promoted to 2.6 h, which can be attributed to the photoinduced fluorescence enhancement effect (PFEE) [11,34]. In this process, adsorbed water molecules passivate surface trap states, allowing free electrons to repopulate from the trap states to the conduction band of the QDs, which results in an increased band-edge radiative recombination [11]. The PFEE is highly dependent on the humidity level, which is predominant with high humidity levels and enhances the PL in a short time (< 15 min). The absorbance of 19-nm-thick QD films was almost the same under the RH of both 35% and 55% after 48 h (Fig. S3).

Table 2
Atomic percentages of Zn, S, Se, In, and P for InP/$ZnSe_xS_{1-x}$/ZnS QD films before and after various exposure conditions.

InP/$ZnSe_xS_{1-x}$/ZnS QD films	Zn / at. %	S / at. %	Se / at. %	In / at. %	P / at. %
UHV before O_2 exposure	25.9	40.5	3.3	7.7	22.5
UHV after O_2 exposure	32.1	33.5	3.1	8.6	22.7
UHV before H_2O exposure	27.1	40.2	3.1	7.5	22.0
UHV after H_2O exposure	30.4	36.1	3.2	7.9	22.5
UHV before O_2 + H_2O exposure	27.9	39.9	3.1	7.5	21.6
UHV after O_2 + H_2O exposure	33.8	33.2	3.0	8.3	21.7

3.2. The effect of QD film's thickness on the PL quenching

Increasing the QD film's thickness (t_{QD}) to 48 nm and 101 nm led to red-shifted and broader PL emissions, indicating more pronounced inter-QD energy transfer, e.g., FRET (Fig. 2 (a) and 2(d)). The spin-coated QD films with different thicknesses using various dispersion concentrations and spin speeds are summarized in Table S1. The PL peak maxima were almost the same after 10 days (Fig. 2(b) and 2(e)), and the $\tau_{1/2}$ extended to 5.9 h and 17.2 h, respectively (Table 1). The PLQY of 48-nm-thick QD films (13.9%) was half that of 100-nm-thick QD films (26.8%) after 240 h (Fig. 2(c) and 2(f)). Notably, the PLQY of 100-nm-thick QD films declined more slowly between 10 and 24 h, which is likely because thicker samples contained more QDs that did not deteriorate at the bottom, maintaining their PL property for a longer period.

3.3. The effect of temperature on the PL quenching

When the 19-nm-thick QD films were stored in the vacuum oven (0.1 mbar, 6% RH) at 22 °C, the emission linewidth did not change significantly, and the PLQY preserved 87% of its initial value after 24 h (Fig. 3 (a)–3(c)). The drop in PLQY was primarily due to air exposure during measuring and a small amount of air remaining in the vacuum oven. Each measurement took approximately 5 min per sample, with three samples tested under each condition. Notably, the PLQY remained stable within 3 h due to the short exposure time, and the PL could be temporarily recovered by vacuum degassing the physisorbed water molecules as the films were put back to the vacuum oven after each measurement [35]. As the vacuum oven temperature was elevated to 50 °C and 100 °C, the PL quenching accelerated, resulting in broader emissions and reducing the PLQY by half and three-fifths, respectively (Fig. 3(d)–3(i)). The $\tau_{1/2}$ of QD films at 22 °C under 55% RH was comparable to that of QD films at 50 °C under vacuum. Heat-facilitated PL quenching can be attributed to the following aspects: Firstly, the difference in the thermal expansion of the core and shell, and increased atomic mobility [36]. This increased the diffusion of defects, and residual oxygen and water are more easily penetrate into the QD core. Secondly, charge carriers convert excess energy into lattice vibrations (phonons) through electron-phonon coupling [37]. The phonon population increases, and multi-phonon emission becomes an efficient relaxation channel, further converting charge carrier energy into heat. Finally, the ligand can be stripped away, leaving behind unpassivated regions on the QD surface [38].

3.4. The effect of oxygen and water exposure on the chemical state changes

To identify the chemical changes in QD films exposed to oxygen and, or, moisture in the dark, XPS survey scans under UHV (Fig. S4) and high-resolution NAP-XPS spectra were recorded for the C 1 s, S 2p, Se 3p, Zn 2p, Zn LMM, Se 3d, P 2p, Zn 3 s, In 3d, and O 1 s electronic states. These measurements were taken from spin-coated 19-nm-thick QD films before exposure, exposure to 3 mbar oxygen and/or 3 mbar moisture at RT and 100 °C, and after exposure under UHV. Fig. 4 illustrates the effect of oxygen exposure. Before oxygen exposure, the main peak positioned at 284.8 eV corresponds to C—C/C—H bonds, while the tail extending to higher binding energies (BE) is associated with the C—S bond of the QD ligand (octanethiol) [39]. After oxygen exposure at RT, additional peaks generated at higher BE values of 287.8 and 288.8 eV were related to C═O and RCOOH groups, respectively (Fig. 4(a)), indicating oxidation of organic contaminants (e.g., alcohols, ethers, ketones, aldehydes) [40,41]. The peak at 286.3 eV likely represents a combination of C—S and C—O bonds due to their proximity. The S 2p spectrum initially exhibited a doublet due to the spin-orbit splitting, $2p_{3/2}$ and $2p_{1/2}$, at 161.9 and 163.1 eV, respectively, which can be assigned to the $ZnSe_xS_{1-x}$/ZnS shell and the QD ligand (Fig. 4(b) inset) [42,43]. An additional doublet appeared with peaks at 168.4 and 169.6 eV after oxygen exposure, which is associated with the formation of SO_x^- owing to oxidation of the QD ligand and/or the shell [44]. The oxidation area increased by 4.4 times after elevating the NAP cell temperature to 100 °C. SO_x^- counted for 6.9 atomic percentage (At.%) of the total S 2p (33.5 at.%, Table 2) after oxygen exposure under UHV. The at.% of elemental core level peaks was calculated by the previously reported Eq. [42].

The peaks at 166.0 and 160.0 eV were attributed to Se $3p_{1/2}$ and Se $3p_{3/2}$, respectively (Fig. 4(b)) [42,45]. Se accounted for 3.7 at.% of the sum of S 2p and Se 3p, so the middle shell can be expressed as $ZnSe_{0.04}S_{0.96}$. Since XPS is highly surface sensitive and Se is covered by an organic ligand layer, the inner shell is likely to be underestimated. The decrease in S at.% after oxygen exposure was likely caused by the stripping of ligands (Table 2). Isolated Zn $2p_{3/2}$ and Zn $2p_{1/2}$ peaks are present at 1022.1 and 1045.1 eV, respectively, with a spin-orbit splitting of 23 eV (Fig. 4(c)) [42,46]. The presence of a small doublet at 1030.3 and 1053.3 eV recorded in the NAP cell was caused by photoelectrons inelastically scattering from oxygen molecules on their way to the detector (Fig. 4(c) inset) [47]. The Zn 2p peak maxima remained the same after oxygen exposure, but the peak area increased by 20.7%, indicating the generation of ZnO [48]. This is consistent with the increasing area ratio (+7.1%) of the highest BE peak of the Zn LMM spectrum at 499.8 eV, which overlaps the peak of ZnS and ZnO (Fig. 4(d) and Table S2) [42,49]. This result is in good agreement with recently reported results from TEM-based chemical analysis [13].

The Se $3d_{3/2}$ and Se $3d_{5/2}$ peaks at 55.3 and 54.3 eV, respectively, with an overlapping spin-orbit separation of 1.0 eV, are comparable to the reported results (Fig. 4(e)) [42,50]. A small peak emerged at 58.8–59.8 eV when exposed to oxygen at 100 °C, corresponding to SeO_2 [50,51], because of increased atomic mobility and longer exposure time. The P 2p spectrum reveals two distinct chemical environments for phosphorus atoms (Fig. 4(f)). The spectrum was fitted using two resolved doublets, with a spin-orbit splitting of 0.9 eV between $2p_{3/2}$ and $2p_{1/2}$. The first dominant doublet that appears at 128.4–129.3 eV is characteristic of InP [52]. The second, more intense doublet is located at higher BE, 133.3–134.2 eV, corresponding to phosphorus in an oxidized environment, likely $InPO_x$ (x = 3 and/or 4), as supported by the literature [10,52]. The presence of $InPO_x$ before oxygen exposure suggests that it was formed during the synthesis or cleaning steps [5,53]. The ratio of oxidized phosphorus atoms ($InPO_x$) to the total phosphorus atoms increased by 6.0% after oxygen exposure. The Zn 3 s spectrum showed no significant change after oxygen exposure. The In $3d_{3/2}$ and In $3d_{5/2}$ peaks, initially at 452.2 and 444.7 eV, respectively, shifted to higher BE (+0.3 eV) after oxygen exposure, indicating the oxidation of In atoms (In_2O_3, Fig. 4(g)) [50,54]. InOOH and $In(OH)_3$ can be excluded as possible oxidation products because the indium source used in this work was indium chloride rather than indium acetate [52,53]. Quantitative data suggest a phosphorus-rich surface, with an In/P ratio close to 0.34 (Table 2), consistent with previous reports [15,55]. The high Zn/In ratio of 3.4 (in as-deposited QD films) supports that the InP core was

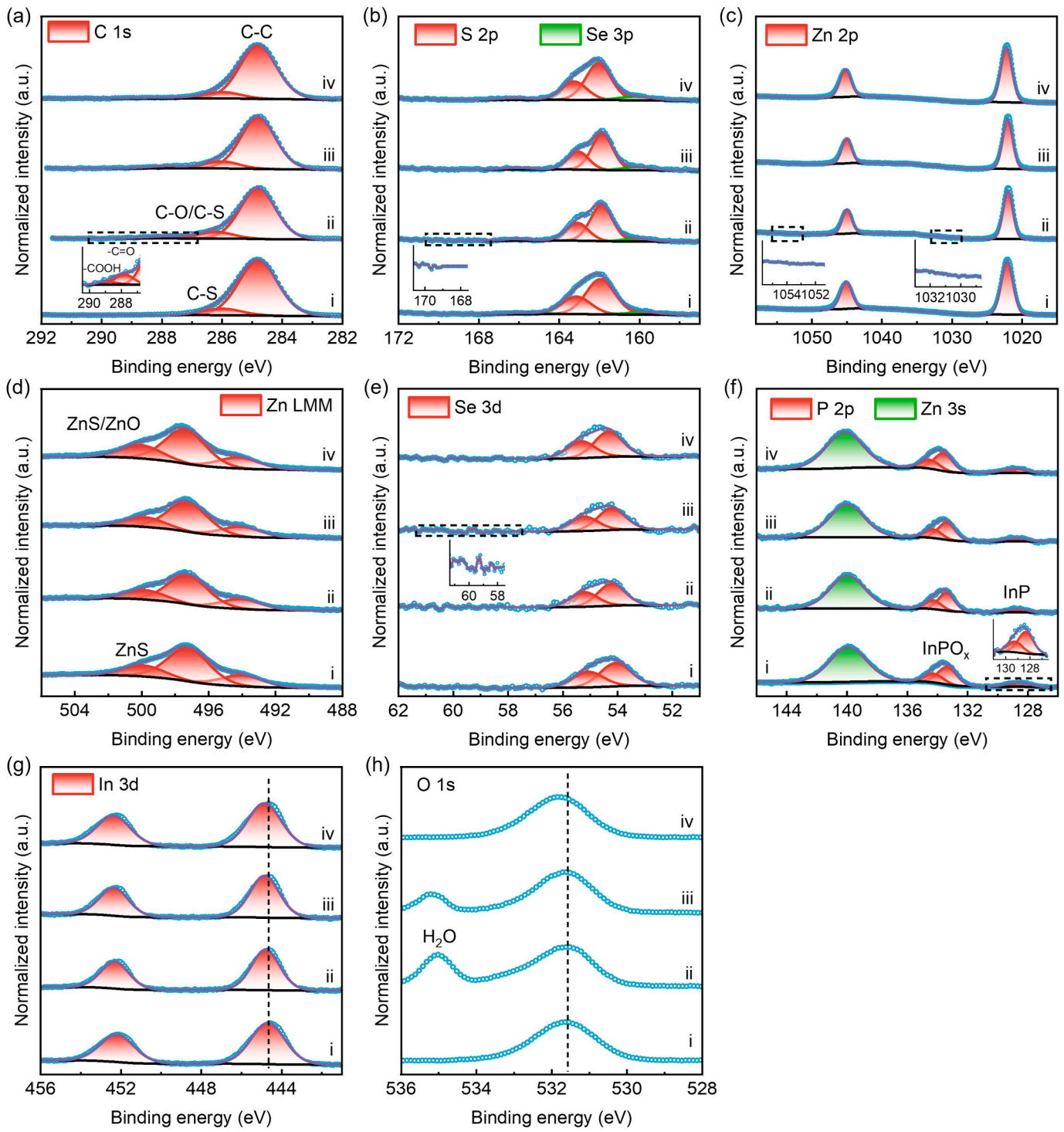

Fig. 5. NAP-XPS spectra of (a) C 1 s, (b) S 2p & Se 3p, (c) Zn 2p, (d) Zn LMM, (e) Se 3d, (f) P 2p & Zn 3 s, (g) In 3d, and (h) O 1 s of 19-nm-thick QD films under different moisture exposure conditions. i – UHV before moisture exposure, ii – 3 mbar moisture exposure at RT, iii – 3 mbar moisture exposure at 100 °C, iv – UHV after moisture exposure. The black, purple, and cyan dotted lines represent the background, envelop, and raw data, respectively. (For interpretation of the references to colour in this figure legend, the reader is referred to the web version of this article.)

covered by the shell with an estimated thickness of about 3.1 nm [56], which is greater than our previously reported TEM result (a core size of 1.8 nm and the total shell thickness of 2.3 nm) [3]. This results from XPS's surface sensitivity, which is much more sensitive to the top layer, leading to a low In at.%. The O 1 s peak shifted to higher BE (+0.2 eV) and the O at.% increased by 12.8% (Fig. 4(h) and Table S3), which is in line with the generation of oxides discussed above.

Subsequently, the degradation of QD films under 3 mbar moisture exposure (RH: ~10%) was studied separately, revealing that water had a minimal impact on the chemical state's change (Fig. 5). The peaks of C═O and COOH were weak, with no observable peaks of SO_x^-, even at 100 °C (Fig. 5(a) and 5(b)). The peak area of Zn 2p remains the same (Fig. 5(c)), and the area ratio of the highest BE peak in the Zn LMM spectrum just slightly increased after water exposure (Fig. 5(d) and Table S2), and Se oxidation was not detected (Fig. 5(e)). The ratio of

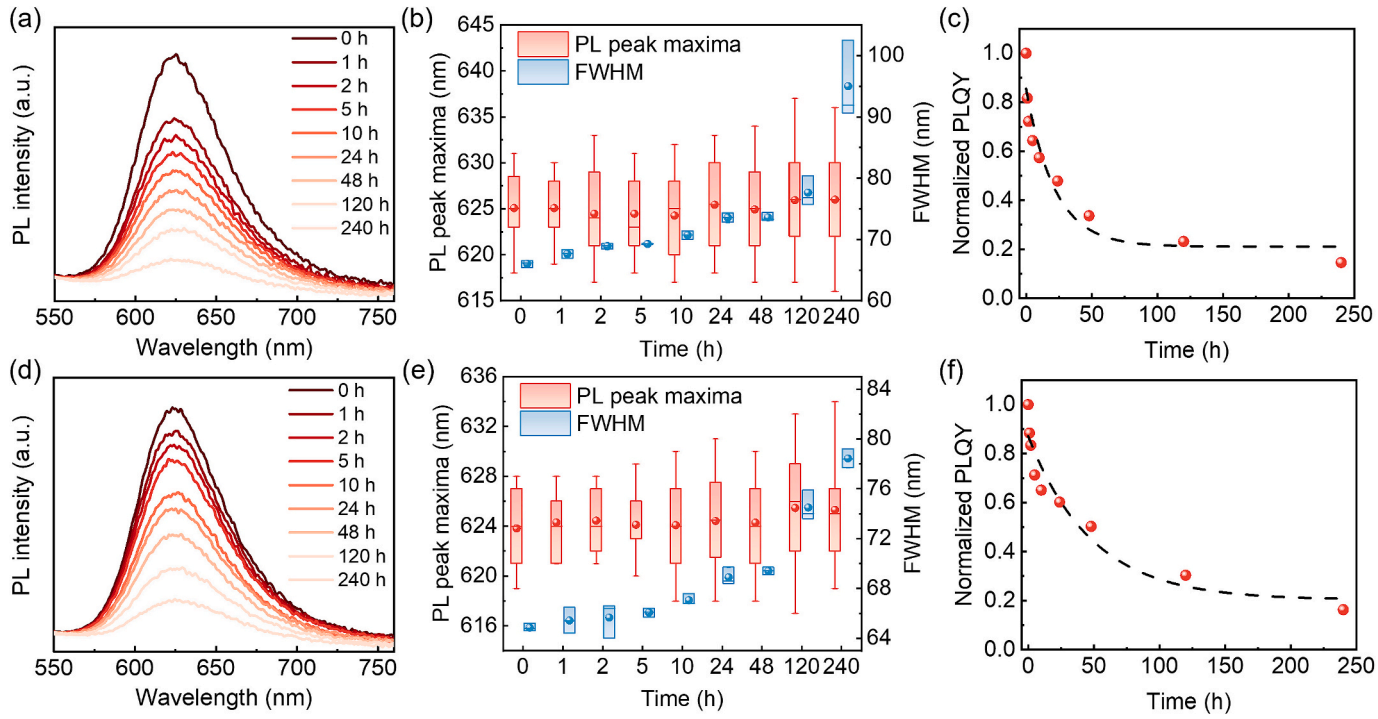

Fig. 6. The evolution of PL emission spectra, corresponding PL peak maxima and FWHM, and normalized PLQY of 19-nm-thick QD films with different thicknesses of PMMA films under the RH of 55% over time at 22 °C. *L* of (a–c) 20 nm and (d–f) 47 nm. The black dashed lines in (c) and (f) are fitting curves of the exponential degradation function.

oxidized phosphorus atoms was almost the same after water exposure (Fig. 5(f) and Table 2), and the shift of the In doublet was insignificant (Fig. 5(g)). The slight increase of oxygen at.% further implies negligible oxidation under moisture exposure (Table S3). The small peak at 535.0 eV in Fig. 5(h) is assigned to gas-phase water above QD films [57]. We found that the combined effects of both oxygen and water exposures (6 mbar) on chemical variations were similar to those of oxygen exposure alone, according to the changes in peak area and position (Fig. S5). The slightly weaker oxidation observed under both oxygen and moisture exposures could be due to the thin capsulation layer of water on QDs, which might alleviate the reaction with oxygen (Table S2 and Table S3).

3.5. The effect of PMMA encapsulation on the PL quenching

To enhance the air stability of QD films, a thin PMMA film with different thicknesses was spin-coated on 19-nm-thick QD films as a protection barrier (Fig. S2 and Table S4). The PL was quenched extremely slowly under 55% RH at 22 °C, sustaining about 50% of the PL with *L* of 20 ± 1 nm and 47 ± 6 nm after 24 h and 48 h, respectively (Fig. 6(a) and 6(d)). FWHM moderately increased to 74 nm and 69 nm, respectively, smaller than that of QD films without PMMA after 48 h (79 nm), and PL peaks remained stable after 10 days (Fig. 6(b) and 6(e)). Weak emissions were still detectable after 5 days (Fig. 6(c) and 6(f)), with the $\tau_{1/2}$ increased by 5 and 12 times (Table 1), respectively. The enhanced air stability of QD films with PMMA layers can be explained by Fick's second law of diffusion [58], the diffusion flux through a thin layer of PMMA can be expressed as.

$$\frac{\partial C}{\partial T} = D\frac{\partial^2 C}{\partial x^2} \tag{2}$$

where *D*, *C*, *x*, and *T* represent the diffusion coefficient, the air concentration in PMMA, diffusion length, and diffusion time, respectively. *D* is dependent on the ambient temperature and PMMA's molecular weight, but independent of *L* [59]. The water vapor and oxygen diffusion coefficients in PMMA are approximately 2.9×10^{-10} m^2/s and 2.0×10^{-12} m^2/s, respectively at RT [60].

Therefore, the total mass of air (M_T) diffused through the PMMA layer at time ($T \gg L^2/D$) can be simplified to [61]:

$$\frac{M_T}{M_\infty} \approx 1 - \frac{8}{\pi^2}\exp\left(-\frac{D\pi^2 T}{4L^2}\right) \tag{3}$$

M_∞ is the equilibrium mass at $T \to \infty$. The PL quenching efficiency (η_Q (T) = 1- Normalized PLQY (T)) is defined as:

$$\eta_Q(T) = kM_T = \eta_{Q,\infty}\left[1 - \mathrm{Aexp}\left(-\frac{T}{\tau}\right)\right] \tag{4}$$

where *k* is a proportionality constant (depends on QD reactivity and density), $\eta_{Q,\infty}$ is the maximum quenching efficiency (when all QDs are quenched), A = $8/\pi^2$, diffusion characteristic time $\tau = 4\ L^2/(D\pi^2)$. The fickian model (eq. (4)) closely matches the experimental data (Fig. S6). η_Q of the QD films encapsulated with 20 nm and 47 nm PMMA barriers increases with exposure time in 55% RH. At all time points, the 47 nm PMMA sample exhibits smaller PL quenching efficiency, confirming that a thicker polymer barrier more effectively retards penetrant transport to the QD surface and improves PL stability. The close agreement between experimental data and diffusion-model fits validates that PL quenching in these samples is diffusion-limited.

4. Conclusions

The PL quenching and chemical state changes in InP/$ZnSe_xS_{1-x}$/ZnS QD films were studied. NAP-XPS results indicated that chemical state changes were primarily caused by oxidation rather than water exposure, forming oxides that include In_2O_3, $InPO_x$, SeO_2, ZnO, and SO_x^-. However, oxygen, water, or heat can introduce permanent trap states, leading to PL quenching. The PL degraded more slowly under higher RH due to the PFEE, which passivated surface trap states and temporarily enhanced the PL. Thicker QD films showed better durability and greater $\tau_{1/2}$ because they contained more QDs, and QDs on the top layer

protected the bottom layer from degradation. Thermal energy stripped surface ligands and increased atomic mobility, expanding the structural deformation between the shell and core and introducing permanent trap states that quenched the PL. Encapsulating with a PMMA barrier layer proved to be an effective strategy to improve the air stability of QD films by reducing the diffusion flux of oxygen and moisture. This study provides insight into the effect of oxygen and/or water on InP/$ZnSe_xS_{1-x}$/ZnS QD films, paving the way to develop more air-stable QD films for InP-based optoelectronic devices like QLEDs.

Declaration of generative AI in scientific writing

The authors declare that no generative AI and AI-assisted technologies were used in the writing process of this manuscript.

CRediT authorship contribution statement

Min Fu: Writing – review & editing, Writing – original draft, Validation, Formal analysis, Data curation, Conceptualization. **Alex Walton:** Writing – review & editing, Formal analysis, Data curation. **Liam Dwyer:** Writing – review & editing, Formal analysis, Data curation. **Xinhui Lan:** Formal analysis, Data curation. **Stephen D. Evans:** Writing – review & editing, Formal analysis. **Kevin Critchley:** Writing – review & editing, Supervision, Project administration, Formal analysis, Conceptualization.

Declaration of competing interest

The authors declare that they have no known competing financial interests or personal relationships that could have appeared to influence the work reported in this paper.

Acknowledgments

M.F. thanks the CSC (No. 202006120057) for funding the research. K.C. thanks the EPSRC (EP/T013753/1) for financial support. This work was supported by the EPSRC National Facility for XPS ("HarwellXPS", EP/Y023587/1, EP/Y023609/1, EP/Y023536/1, EP/Y023552/1, and EP/Y023544/1) and the Henry Royce Institute for Advanced Materials, funded through EPSRC grants EP/R00661X/1, EP/S019367/1, EP/P025021/1, and EP/P025498/1. We thank BRG Johnson for his help in 3D printing parts to adapt experiments to commercial instruments. The authors acknowledge RJ Bushby for his assistance in the synthesis of QDs.

Appendix A. Supplementary data

Supplementary data to this article can be found online at https://doi.org/10.1016/j.rechem.2026.103144.

Data availability

Data related to this paper are available from https://doi.org/10.5518/1794 [62].

References

[1] B. Cook, Q.F. Liu, M.G. Gong, D. Ewing, M. Casper, A. Stramel, J. Wu, Quantum dots-facilitated printing of ZnO nanostructure photodetectors with improved performance, ACS Appl. Mater. Interfaces 9 (2017) 23189–23194.
[2] T.M. Eggenhuisen, Y. Galagan, A. Biezemans, T. Slaats, W.P. Voorthuijzen, S. Kommeren, S. Shanmugam, J.P. Teunissen, A. Hadipour, W.J.H. Verhees, S. C. Veenstra, M.J.J. Coenen, J. Gilot, R. Andriessen, W.A. Groen, High efficiency, fully inkjet printed organic solar cells with freedom of design, J. Mater. Chem. A 3 (2015) 7255–7262.
[3] M. Fu, J.J. Santaella, S.D. Evans, K. Critchley, Inkjet printing of cadmium-free quantum dots-based electroluminescent devices, ACS Appl. Mater. Interfaces 17 (2025) 22952–22962.
[4] S. Click, S. Rosenthal, Synthesis, surface chemistry, and fluorescent properties of InP quantum dots, Chem. Mater. 35 (2023) 822–836.
[5] Y.-H. Won, O. Cho, T. Kim, D.-Y. Chung, T. Kim, H. Chung, H. Jang, J. Lee, D. Kim, E. Jang, Highly efficient and stable InP/ZnSe/ZnS quantum dot light-emitting diodes, Nature 575 (2019) 634–638.
[6] J. Muller, J.M. Lupton, A.L. Rogach, J. Feldmann, D.V. Talapin, H. Weller, Air-induced fluorescence bursts from single semiconductor nanocrystals, Appl. Phys. Lett. 85 (2004) 381–383.
[7] W. van Sark, P. Frederix, D.J. Van den Heuvel, H.C. Gerritsen, A.A. Bol, J.N.J. van Lingen, C.D. Donega, A. Meijerink, Photooxidation and photobleaching of single CdSe/ZnS quantum dots probed by room-temperature time-resolved spectroscopy, J. Phys. Chem. B 105 (2001) 8281–8284.
[8] W. van Sark, P. Frederix, A.A. Bol, H.C. Gerritsen, A. Meijerink, Blueing, bleaching, and blinking of single CdSe/ZnS quantum dots, Chemphyschem 3 (2002) 871–879.
[9] R. Brown, M. Gallagher, D. Fairbrother, Z. Rosenzweig, Synthesis and degradation of cadmium-free InP and InPZn/ZnS quantum dots in solution, Langmuir 34 (2018) 13924–13934.
[10] X. Duan, J. Ma, W. Zhang, P. Liu, H. Liu, J. Hao, K. Wang, L. Samuelson, X. Sun, Study of the interfacial oxidation of InP quantum dots synthesized from tris (dimethylamino)phosphine, ACS Appl. Mater. Interfaces 15 (2023) 1619–1628.
[11] K. Pechstedt, T. Whittle, J. Baumberg, T. Melvin, Photoluminescence of colloidal CdSe/ZnS quantum dots: the critical effect of water molecules, J. Phys. Chem. C 114 (2010) 12069–12077.
[12] Y. Li, W. Zhang, K. Li, Y. Yao, J. Niu, Y. Chen, Oxidative dissolution of polymer-coated CdSe/ZnS quantum dots under UV irradiation: mechanisms and kinetics, Environ. Pollut. 164 (2012) 259–266.
[13] H. Baek, S. Kang, J. Heo, S. Choi, R. Kim, K. Kim, N. Ahn, Y. Yoon, T. Lee, J. Chang, K. Lee, Y. Park, J. Park, Insights into structural defect formation in individual InP/ZnSe/ZnS quantum dots under UV oxidation, Nat. Commun. 15 (2024) 1671.
[14] M.D. Tessier, D. Dupont, K. De Nolf, J. De Roo, Z. Hens, Economic and size-tunable synthesis of InP/ZnE (E = S, se) colloidal quantum dots, Chem. Mater. 27 (2015) 4893–4898.
[15] P. Yu, S. Cao, Y.L. Shan, Y.H. Bi, Y.Q. Hu, R.S. Zeng, B.S. Zou, Y.J. Wang, J.L. Zhao, Highly efficient green InP-based quantum dot light-emitting diodes regulated by inner alloyed shell component, Light: Sci. Appl. 11 (2022) 162.
[16] P. Liu, Y.J. Lou, S.H. Ding, W.D. Zhang, Z.H. Wu, H.C. Yang, B. Xu, K. Wang, X. W. Sun, Green InP/ZnSeS/ZnS Core multi-shelled quantum dots synthesized with aminophosphine for effective display applications, Adv. Funct. Mater. 31 (2021) 2008453.
[17] J. Jo, S. Lee, H. Heo, K. Lee, Stability enhancement of InP quantum dot/poly (methyl methacrylate) nanocomposites for light-emitting diode applications by grafting thermoresponsive poly(N-isopropylacrylamide), J. Mater. Chem. C 9 (2021) 14606–14612.
[18] Y. Xie, C. Geng, X. Liu, S. Xu, W. Xing, X. Zhang, Z. Zhang, Y. Zhang, W. Bi, Synthesis of highly stable quantum-dot silicone nanocomposites via *in situ* zinc-terminated polysiloxane passivation, Nanoscale 9 (2017) 16836–16842.
[19] Y. Chang, X. Yao, Z. Zhang, D. Jiang, Y. Yu, L. Mi, H. Wang, G. Li, D. Yu, Y. Jiang, Preparation of highly luminescent $BaSO_4$ protected CdTe quantum dots as conversion materials for excellent color-rendering white LEDs, J. Mater. Chem. C 3 (2015) 2831–2836.
[20] S. Lee, C. Sakong, B. Ju, K. Cho, Enhancing the reliability of InP-based QD color conversion layer through a uniform organic encapsulation layer via inkjet printing, Org. Electron. 135 (2024) 107136.
[21] Y. Wang, H. Wu, H. Gao, Q. Ren, K. Ni, S. Liu, W. Ma, J. Wang, Z. Liu, R. Liu, Hybrid thin film encapsulation for improving the stability of PbS quantum dot solar cells, Small 20 (2024) 2404984.
[22] U. Ali, K. Abd Karim, N. Buang, A review of the properties and applications of poly (methyl methacrylate) (PMMA), Polym. Rev. 55 (2015) 678–705.
[23] X. Dai, Z. Zhang, Y. Jin, Y. Niu, H. Cao, X. Liang, L. Chen, J. Wang, X. Peng, Solution-processed, high-performance light-emitting diodes based on quantum dots, Nature 515 (2014) 96–99.
[24] I. Suárez, H. Gordillo, R. Abargues, S. Albert, J. Martínez-Pastor, Photoluminescence waveguiding in CdSe and CdTe QDs-PMMA nanocomposite films, Nanotechnology 22 (2011) 435202.
[25] H. Roh, D. Ko, D.Y. Shin, J.H. Chang, D. Hahm, W.K. Bae, C. Lee, J.Y. Kim, J. Kwak, Enhanced performance of pixelated quantum dot light-emitting diodes by inkjet printing of quantum dot-polymer composites, Adv. Opt. Mater. 9 (2021) 2002129.
[26] J.F. Young, Humidity control in the laboratory using salt solutions—a review, J. Appl. Chem. 17 (1967) 241–245.
[27] J.H. Jo, J.H. Kim, K.H. Lee, C.Y. Han, E.P. Jang, Y.R. Do, H. Yang, High-efficiency red electroluminescent device based on multishelled InP quantum dots, Opt. Lett. 41 (2016) 3984–3987.
[28] C.R. Kagan, C.B. Murray, M.G. Bawendi, Long-range resonance transfer of electronic excitations in close-packed CdSe quantum-dot solids, Phys. Rev. B 54 (1996) 8633–8643.
[29] H. Zhang, Q. Su, S. Chen, Suppressing Forster resonance energy transfer in close-packed quantum-dot thin film: toward efficient quantum-dot light-emitting diodes with external quantum efficiency over 21.6%, Adv. Opt. Mater. 8 (2020) 1902092.
[30] K. Wegner, F. Dussert, D. Truffier-Boutry, A. Benayad, D. Beal, L. Mattera, W. Ling, M. Corrière, P. Reiss, Influence of the Core/Shell structure of indium phosphide based quantum dots on their photostability and cytotoxicity, Front. Chem. 7 (2019) 466.
[31] A. Tran, R. Valleix, F. Reveret, L. Frezet, F. Cisnetti, D. Boyer, Encapsulation of InP/ZnS quantum dots into MOF-5 matrices for solid-state luminescence: ship in the bottle and bottle around the ship methodologies, Materials 17 (2024) 3155.

[32] Z. Yang, G. Lin, J. Bai, L. Li, Y. Zhu, L. He, Z. Jiang, W. Wu, X. Yu, F. Li, W. Li, Inkjet-printed blue InP/ZnS/ZnS quantum dot light-emitting diodes, Chem. Eng. J. 450 (2022) 138413.
[33] E. Janke, N. Williams, C. She, D. Zherebetskyy, M. Hudson, L. Wang, D. Gosztola, R. Schaller, B. Lee, C. Sun, G. Engel, D. Talapin, Origin of broad emission spectra in InP quantum dots: contributions from structural and electronic disorder, J. Am. Chem. Soc. 140 (2018) 15791–15803.
[34] M. Jones, J. Nedeljkovic, R. Ellingson, A. Nozik, G. Rumbles, Photoenhancement of luminescence in colloidal CdSe quantum dot solutions, J. Phys. Chem. B 107 (2003) 11346–11352.
[35] S. Cordero, P. Carson, R. Estabrook, G. Strouse, S. Buratto, Photo-activated luminescence of CdSe quantum dot monolayers, J. Phys. Chem. B 104 (2000) 12137–12142.
[36] Y. Zhao, C. Riemersma, F. Pietra, R. Koole, C. Donegá, A. Meijerink, High-temperature luminescence quenching of colloidal quantum dots, ACS Nano 6 (2012) 9058–9067.
[37] S. Savchenko, A. Vokhmintsev, M. Karabanalov, Y. Zhang, A. Henaish, A. Neogi, I. Weinstein, Thermally assisted optical processes in InP/ZnS quantum dots, Phys. Chem. Chem. Phys. 26 (2024) 18727–18740.
[38] P. Schiettecatte, L. Giordano, B. Cruyssaert, G. Bonifas, N. De Vlamynck, H. Van Avermaet, Q. Zhao, A. Vantomme, C. Nayral, F. Delpech, Z. Hens, Enhanced surface passivation of InP/ZnSe quantum dots by zinc acetate exposure, Chem. Mater. 36 (2024) 5996–6005.
[39] J. Sette-Ducati, R. Donnelly, A. Molski, E. Robinson, E. Canning, D. Williams, E. Landis, L. Avila-Bront, Understanding the two-dimensional mixing behavior of 1-Naphthalenethiol and Octanethiol, J. Phys. Chem. C 127 (2023) 6531–6542.
[40] Y. Bourlier, M. Bouttemy, O. Patard, P. Gamarra, S. Piotrowicz, J. Vigneron, R. Aubry, S. Delage, A. Etcheberry, Investigation of InAlN layers surface reactivity after thermal annealings: a complete XPS study for HEMT, ECS J. Solid State Sci. Technol. 7 (2018) P329–P338.
[41] J. Landoulsi, M.J. Genet, S. Fleith, Y. Touré, I. Liascukiene, C. Méthivier, P. G. Rouxhet, Organic adlayer on inorganic materials: XPS analysis selectivity to cope with adventitious contamination, Appl. Surf. Sci. 383 (2016) 71–83.
[42] V. Krishna, M. Mahesha, XPS analysis of $ZnS_{0.4}Se_{0.6}$ thin films deposited by spray pyrolysis technique, J. Electron Spectrosc. Relat. Phenom. 249 (2021) 147072.
[43] K. Jiang, W. Huang, T. Song, P. Wu, W. Wang, Q. Chen, M. Wang, G. Guo, Photobreeding heterojunction on semiconductor materials for enhanced photocatalysis, Adv. Funct. Mater. 33 (2023) 2304351.
[44] J. Chauvin, D. Pratt, On the reactions of thiols, sulfenic acids, and Sulfinic acids with hydrogen peroxide, Angew. Chem. Int. Ed. 56 (2017) 6255–6259.
[45] J. Shallenberger, N. Hellgren, Zinc selenide analyzed by XPS, Surf. Sci. Spectra 27 (2020) 014020.
[46] L. Ding, J. Zhao, Z. Bao, S. Zhang, H. Shi, J. Liu, G. Wang, X. Peng, X. Zhong, J. Wang, Synchronous generation of green oxidants H_2O_2 and O_3 by using a heterojunction bifunctional ZnO/ZnS@C electrocatalyst, J. Mater. Chem. A 11 (2023) 3454–3463.
[47] A. Regoutz, G. Kerherve, I. Villar-Garcia, C.K. Williams, D.J. Payne, The influence of oxygen on the surface interaction between CO2 and copper studied by ambient pressure X-ray photoelectron spectroscopy, Surf. Sci. 677 (2018) 121–127.
[48] N. Dengo, A.F. De Fazio, M. Weiss, R. Marschall, P. Dolcet, M. Fanetti, S. Gross, Thermal evolution of ZnS nanostructures: effect of oxidation phenomena on structural features and photocatalytical performances, Inorg. Chem. 57 (2018) 13104–13114.
[49] N. Hellgren, M. Steves, J. Shallenberger, S. O'Boyle, E. Mellott, A. Noble, Effect of etching on the oxidation of zinc selenide surfaces characterized by X-ray photoelectron spectroscopy, Appl. Surf. Sci. 528 (2020) 146604.
[50] L.L. Kazmerski, O. Jamjoum, P.J. Ireland, S.K. Deb, R.A. Mickelsen, W. Chen, Initial oxidation of $CuInSe_2$, J. Vac. Sci. Technol. 19 (1981) 467–471.
[51] R. Würz, M. Rusu, T. Schedel-Niedrig, M. Lux-Steiner, H. Bluhm, M. Hävecker, E. Kleimenov, A. Knop-Gericke, R. Schlögl, In situ X-ray photoelectron spectroscopy study of the oxidation of $CuGaSe_2$, Surf. Sci. 580 (2005) 80–94.
[52] H. Virieux, M. Le Troedec, A. Cros-Gagneux, W. Ojo, F. Delpech, C. Nayral, H. Martinez, B. Chaudret, InP/ZnS nanocrystals: coupling NMR and XPS for fine surface and interface description, J. Am. Chem. Soc. 134 (2012) 19701–19708.
[53] D. Granada-Ramirez, J. Arias-Cerón, M. Pérez-González, J. Luna-Arias, A. Cruz-Orea, P. Rodríguez-Fragoso, J. Herrera-Pérez, M. Gómez-Herrera, S. Tomás, F. Vázquez-Hernández, A. Durán-Ledezma, J. Mendoza-Alvarez, Chemical synthesis and optical, structural, and surface characterization of InP-In_2O_3 quantum dots, Appl. Surf. Sci. 530 (2020) 147294.
[54] J. Jo, J. Kim, S. Lee, H. Jang, D. Jang, J. Lee, K. Park, Y. Choi, C. Ha, H. Yang, Photostability enhancement of InP/ZnS quantum dots enabled by In_2O_3 overcoating, J. Alloys Compd. 647 (2015) 6–13.
[55] W. Chen, W. Wang, L. Sun, S. Chen, Q. Yan, T. Guo, X. Zhou, C. Wu, Y. Zhang, Synthesis and characterization of InP/ZnSe/ZnS quantum dots for photo-emissive color conversion, Opt. Mater. Express 12 (2022) 1717–1730.
[56] H. Byun, J. Lee, H. Yang, Solvothermal synthesis of InP quantum dots and their enhanced luminescent efficiency by post-synthetic treatments, J. Colloid Interface Sci. 355 (2011) 35–41.
[57] C. Dinh, A. Jain, F. de Arquer, P. De Luna, J. Li, N. Wang, X. Zheng, J. Cai, B. Gregory, O. Voznyy, B. Zhang, M. Liu, D. Sinton, E. Crumlin, E. Sargent, Multi-site electrocatalysts for hydrogen evolution in neutral media by destabilization of water molecules, Nat. Energy 4 (2019) 107–114.
[58] A. Fick, On liquid diffusion, J. Membr. Sci. 100 (1995) 33–38.
[59] M. Klinger, L. Tolbod, K. Gothelf, P. Ogilby, Effect of polymer cross-links on oxygen diffusion in glassy PMMA films, ACS Appl. Mater. Interfaces 1 (2009) 661–667.
[60] P.E. Keller, R.T. Kouzes, Water vapor permeation in plastics, Pacific Northwest National Lab.(PNNL), Richland, WA (United States), 2016.
[61] J. Crank, The Mathematics of Diffusion, Oxford university press, 1979.
[62] M. Fu, A. Walton, L. Dwyer, X. Lan, S.D. Evans, K. Critchley, The photoluminescence degradation of InP/ZnSexS1-x/ZnS quantum dot films [dataset], University of Leeds, 2025, https://doi.org/10.5518/1794.